JOURNAL OF PROPULSION AND POWER
Vol. 10, No. 5, Sept.–Oct. 1994

Study on Computing Separating Flows Within a Diffusing Inlet S-Duct

B. H. Anderson,* D. R. Reddy,† and K. Kapoor‡
NASA Lewis Research Center, Cleveland, Ohio 44135

A three-dimensional implicit full Navier-Stokes (FNS) analysis and a three-dimensional reduced Navier-Stokes (RNS) initial value space marching solution technique have been applied to a class of separated flow problems within a diffusing S-duct configuration characterized as vortex-liftoff. Both the FNS and the RNS solution technique were able to capture the overall flow physics of vortex liftoff, and gave remarkably similar results which agreed reasonably well with the experimental performance data. However, the FNS and RNS also consistently predicted separation further downstream in the M2129 inlet S-duct than was indicated by experimental data. The separated region associated with vortex liftoff in M2129 inlet S-duct increased in size as the inlet mass flow increased, although the radial extent of the reverse flow region remained very small. Since the reverse flow velocity was also very small, the separated flow in the M2129 S-duct might be regarded as incipient. This, along with the fact that the RNS analysis was able to capture the topology of vortex liftoff, indicates that the parabolized form of the Navier-Stokes equations are appropriate for separated flows represented by the M2129 inlet S-duct.

Nomenclature

A_i	=	inlet throat area
C_f	=	wall skin friction coefficient
DC_{60}	=	distortion descriptor defined as the maximum $(Pt_{ave} - Pt_{min})/q_{ave}$ in any 60.0-deg sector
D_i	=	inlet throat diameter
L	=	length of inlet duct
M_i	=	inlet throat Mach number
Pt_{ave}	=	average total pressure
Pt_{max}	=	maximum total pressure
Pt_{min}	=	minimum total pressure in any sector of extent 60.0 deg
Pt_0	=	freestream total pressure
q_{ave}	=	average dynamic pressure at the engine face
R_{ef}	=	engine face radius
Rey	=	Reynolds number based on throat diameter
R_i	=	inlet throat radius
S_{sep}	=	separation location measured in terms of arc length distance along the duct centerline
Tt_0	=	freestream total temperature
X, Y, Z	=	primary Cartesian coordinates
X_{cl}, Y_{cl}, Z_{cl}	=	Cartesian coordinates along inlet centerline
ΔZ_{cl}	=	centerline offset distance
δ_{ef}	=	fractional distance across engine face
θ	=	polar angle referenced to inlet centerline

Introduction

MODERN tactical aircraft are required to be maneuverable at subsonic, transonic, and supersonic speeds, without giving up good cruise performance. Consequently, proper integration of the engine inlet with the airframe is of paramount importance. Design for optimum airframe-inlet integration has the following goals: 1) to minimize approach flow angularity with respect to the inlet cowl lip; 2) to deliver uniform, high-pressure recovery flow to the inlet face; 3) to prevent or minimize vortex, wake, and boundary-layer ingestion by the inlet throughout the flight envelope; 4) to reduce FOD/hot gas ingestion by the inlet; and finally 5) to minimize the potential for flowfield interference from weapon carriage/firing, landing gear deployment, tanks, pods, or other hardware. The integrated inlet design must provide high-pressure recovery to maintain the desired thrust levels, and low flow distortion consistent with stable engine operation.

Engine face flow distortion is one of the most troublesome and least understood problems for designers of modern inlet engine systems.[1,2] One issue is that there are numerous sources of flowfield distortion that are ingested by the inlet or generated within the inlet duct itself. Among these sources are 1) flow separation at the cowl lip during maneuvering flight, 2) flow separation on the compression surfaces due to shock wave boundary-layer interactions, 3) spillage of the fuselage boundary layer into the inlet duct, 4) ingestion of aircraft vortices and wakes emanating from upstream disturbances, and 5) secondary flow and possibly flow separation within the inlet duct itself. Most aircraft have experienced one or more of these types of problems during development, particularly at high Mach numbers and/or extreme maneuver conditions, such that flow distortion at the engine face exceeded allowable surge limits. Such compatibility problems were encountered in the early versions of the B70, the F-111, the F-14, the MIG-25, the Tornado, and the Airbus A300 to name a few examples.

Flow separation in diffusing S-duct geometries characterized as vortex liftoff has been studied by Harlof et al.[3] using full Navier-Stokes (FNS) analysis techniques and by Anderson and Farokhi[4] using an reduced Navier-Stokes (RNS) approach. This class of separated flows are very common within inlet ducts, and are a major cause of pressure loss and distortion at the engine face, particularly circumferential distortion. A RNS solution technique using FLARE approximations[4] has been shown to physically describe the topological and topographical structure of flow separation associated with vortex liftoff, however, no detailed comparative study has been made between FNS and RNS viscous analyses for this phenomenon over a wide range of inlet flow conditions.

Received May 5, 1993; presented as Paper 93-2154 at the AIAA/SAE/ASME/ASEE 29th Joint Propulsion Conference and Exhibit, Monterey, CA, June 28–30, 1993; revision received Jan. 4, 1994; accepted for publication Jan. 26, 1994.

*Senior Research Scientist. Member AIAA.
†Senior NRC Fellow. Member AIAA.
‡Branch Chief. Member AIAA.

This article examines the phenomena of vortex liftoff using both FNS and RNS solution techniques, each with an algebraic eddy viscosity turbulence model. Specifically, the goals of this article are as follows:

1) To examine the capability of the FNS and RNS analyses to describe the phenomena of vortex liftoff over a wide range of inlet flow conditions.

2) To characterize the phenomena of vortex liftoff and identify uncertainties in the analysis of this interaction.

3) To examine the prediction of the relevant inlet performance parameters of total pressure recovery and various engine face distortion descriptors relative to experimental measurements.

Theoretical Background

Reduced Navier-Stokes Analysis

Three-dimensional viscous subsonic flows in complex inlet duct geometries are investigated by a numerical procedure which allows solution by spatial forward-marching integration, utilizing flow approximations from the velocity-decomposition approach of Briley and McDonald.[5,6] The goal of this approach is to achieve a level of approximation that will yield accurate flow predictions, while reducing the labor below that needed to solve the full Navier-Stokes equations. The governing equations for this approach have been given previously for orthogonal coordinates, and the approach has been applied successfully to problems whose geometries can be fitted conveniently with orthogonal coordinate systems. However, geometries encountered in typical subsonic inlet ducts cannot be treated easily using orthogonal coordinates, and this led to an extension of this approach by Levy et al.,[7] to treat ducted geometries with nonorthogonal coordinates. In generalizing the geometry formulation, Anderson[8] extended the analysis to cover ducted geometries defined by an externally generated gridfile, such that it allowed for 1) reclustering the existing gridfile, 2) redefining the centerline space curve, and 3) altering the cross-sectional shape and area distribution without returning to the original gridfile. This version of the three-dimensional RNS computer code is called RNS3D. The turbulence model used in RNS3D is that of McDonald and Camarata[9] that employs an eddy-viscosity formulation for the Reynolds stresses.

The analysis as presented here is applicable only when the primary velocity is not negative. Since "small" regions of reverse flow can arise in curved inlet ducts, the numerical method is locally modified to permit forward marching when the flow contains small regions of reverse flow. The technique used follows Reyhner and Flugge-Lotz,[10] by adding small artificial convection at grid points where the primary flow is reversed. This is known as the FLARE approximation, after the authors.[10] For thin regions of reverse flow, although the area of flow separation can be very large compared to the passage itself, the technique permits the analysis to proceed downstream beyond reattachment, confining the FLARE approximation to the separated region.

Full Navier-Stokes Analysis

The PARC3D[11] code, selected for this study, solves the full three-dimensional, Reynolds-averaged, Navier-Stokes equations in strong conservation form with the Beam and Warming approximate factorization algorithm, by advancing an initial solution in time to steady state. The implicit scheme uses central differencing for a curvilinear set of coordinates. The code was originally developed as AIR3D by Pulliam and Steger.[12] Pulliam[13] later added the Jameson[14] artificial dissipation and called the code ARC3D. Copper[11] adapted the ARC3D computer code for internal propulsion applications and named the code PARC3D. To simplify the solution of the block pentadiagonal system of discretized equations, the block implicit operators were diagonalized by decomposing the flux Jacobians, resulting in a scalar pentadiagonal system. The loss of time consistency, caused by the inconsistent differentiation of the decomposed Jacobians, does not affect the spatial accuracy of the steady-state solution.[15] The turbulence model used in PARC3D is the Baldwin-Lomax[16] model that is also an algebraic eddy viscosity model. In the present computations, the turbulence model has been modified to improve the simulation of the reverse flow regions based on the study by Deiwert.[17] In the regions of reverse flow, the inner layer is replaced with the outer model that extends all the way to the wall. In the absence of reverse flow, the conventional Baldwin-Lomax turbulence model is used.

Results and Discussions

The experiment on which this study is based comes from the AGARD Fluid Dynamics Panel Working Group 13 numerical subgroup test case 3.[18] AGARD Working Group 13 was formed to investigate the subject of inlet performance using results from both experimental and computational techniques. One of the test cases chosen by Working Group 13 was the DRA inlet model M2129, which is a circular inlet followed by an S-duct diffuser. This set of experimental data was chosen because it provided information on the separation characteristics over a large inlet mass flow range. The M2129 inlet duct geometry is shown in Fig. 1 and was based on a study by Willmer et al.[19] and by Gibb and Jackson.[20] The centerline of the inlet defined in terms of the coordinate system shown in Fig. 1 is given by

$$Z_{cl} = -\Delta Z_{cl}[1 - \cos(\pi X_{cl}/L)] \tag{1}$$

and the radius distribution measured perpendicular to the duct centerline is described by

$$\left(\frac{R - R_i}{R_{ef} - R_i}\right) = 3\left(1 - \frac{X_{cl}}{L}\right)^4 - 4\left(1 - \frac{X_{cl}}{L}\right)^3 + 1 \tag{2}$$

For the purposes of the calculations, the M2129 S-duct was nondimensionalized with respect to the throat radius, thus $R_i = 1.0$, $R_{ef} = 1.183$, $L = 7.10$, and $\Delta Z_{cl} = 2.13$.

A polar grid topology was chosen for the M2129 S-duct which consisted of 49 radial, 49 circumferential, and 61 streamwise nodal points in the half-plane, for a total number of 146,461 grid points (Fig. 1). The internal grid was constructed such that the transverse computational plane was perpendicular to the duct centerline. Grid clustering was used in the radial direction in order to redistribute the nodal points to resolve the high shear regions near the wall. The radial spacing was chosen to provide a nominal y^+ of 0.5 at the first grid point away from the wall. A study on the effects of near-wall resolution y^+ on the separation characteristics of vortex liftoff and the engine face flowfield was performed by Anderson and Farokhi.[4] The flow in the inlet was considered turbulent throughout, and the inflow boundary-layer thickness δ/R_i was 0.012. This provided approximately the same inlet mass flow as in the experiment. However, it must be

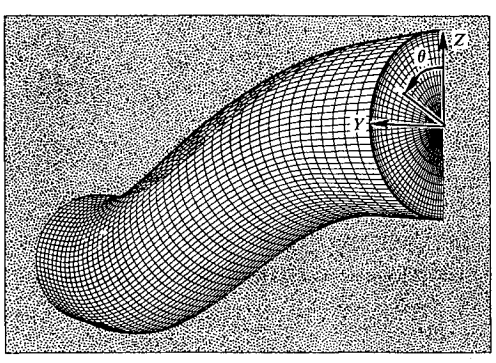

Fig. 1 Geometry definition for the M2129 inlet S-duct.

Table 1 Initial conditions and summary of inlet performance for the M2129 inlet S-duct

Mach no.	Reynolds no.	RNS analysis			FNS analysis		
		S_{sep}/R_i	$\overline{Pt}_{ef}/Pt_0$	DC_{60}	S_{sep}/R_i	$\overline{Pt}_{ef}/Pt_0$	DC_{60}
0.100	0.301 × 10e6	4.456	0.999	0.320	—	—	—
0.200	0.594 × 10e6	4.897	0.997	0.273	4.893	0.996	0.229
0.300	0.873 × 10e6	5.109	0.994	0.254	—	—	—
0.412	1.158 × 10e6	5.323	0.990	0.254	4.456	0.987	0.321
0.500	1.385 × 10e6	5.109	0.985	0.267	—	—	—
0.600	1.577 × 10e6	4.675	0.979	0.297	—	—	—
0.700	1.723 × 10e6	4.236	0.971	0.348	—	—	—
0.794	1.848 × 10e6	3.794	0.962	0.416	4.674	0.958	0.441

Table 2 AGARD test cases, initial conditions

Test case 3.1	
Total pressure	Pt_0 = 29.889 in.Hg
Total temperature	Tt_0 = 293 K
Throat Mach number	M_i = 0.794
Throat diameter	D_i = 5.071 in.
Throat area	A_i = 25.254 in.^{2}
Reynolds number (based on D_i)	Rey = 1.848 × 10^6
Test case 3.2	
Total pressure	Pt_0 = 29.865 in.Hg
Total temperature	Tt_0 = 293 K
Throat Mach number	M_i = 0.412
Throat diameter	D_i = 5.071 in.
Throat area	A_i = 25.254 in.^{2}
Reynolds number (based on D_i)	Rey = 1.158 × 10^6
Test case 3.3	
Total pressure	Pt_0 = 29.889 in.Hg
Total temperature	Tt_0 = 293 K
Throat Mach number	M_i = 0.200
Throat diameter	D_i = 5.071 in.
Throat area	A_i = 25.254 in.^{2}
Reynolds number (based on D_i)	Rey = 0.594 × 10^6

understood that the experimental inlet mass was not very accurate since it was determined using a standard 72 probe engine face rake.

A summary of the inlet test conditions used in this study is presented in Table 1, and covers the nominal inlet throat Mach number range from 0.1 to 0.8. It also includes the AGARD test case 3.1 and 3.2 test conditions defined in Table 2.

For the purposes of examining the separation characteristics within the M2129 inlet S-duct with both FNS and RNS solution techniques at a low inlet throat Mach number, a third test case was also defined in Table 2.

Presented in Table 1 is the computed location of separation S_{sep} from both the FNS and RNS analyses (as measured in terms of the arc length along the inlet centerline), the area-averaged engine face total pressure recovery $\overline{Pt}_{ef}/Pt_0$, and the DC_{60} engine face distortion, both determined from the flow values on the computational mesh.

The initial flowfield for the FNS computations was obtained from the RNS solution. In addition, the imposition of the inlet boundary layer, which was held fixed during the time-marching FNS solution, was straightforward since the initial flowfield had the same initial inlet boundary layer. The average computing time for the RNS solutions was 4.2 min on the Cray X-MP, while the average computing time for the FNS solution technique was 300 min on the Cray Y-MP, starting from the RNS solution as the initial flowfield guess. A FNS computation was also performed with uniform free-stream flow as the initial guess for the flowfield, with the boundary-layer profile unchanged. The computational time for this case was about the same as the RNS solution as the initial guess.

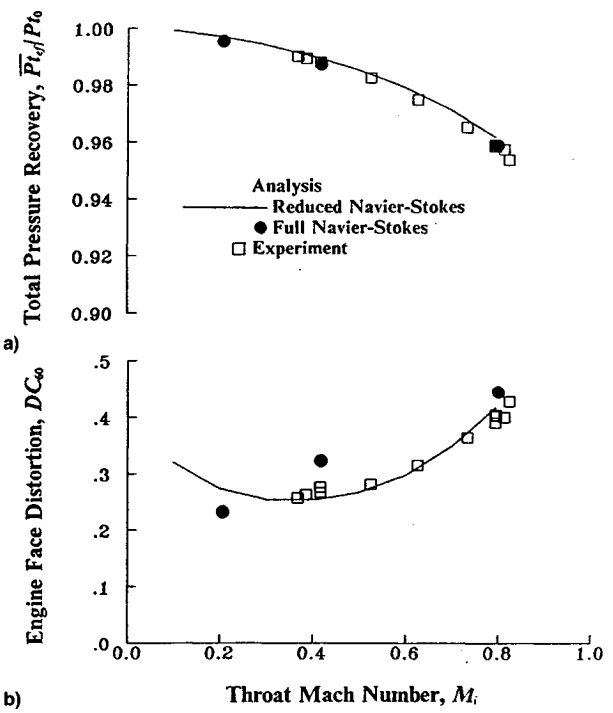

Fig. 2 Effect of inlet throat Mach number on engine face: a) total pressure recovery, Pt_{ef}/Pt_0 and b) engine face DC_{60} distortion, M2129 inlet S-duct.

Figures 2a and 2b present the effect of inlet throat Mach on the area-averaged total pressure recovery $\overline{Pt}_{ef}/Pt_0$ and DC_{60} engine face distortion as determined from the RNS, FNS solution technique, and experimental measurements. The two solution techniques gave essentially the same total pressure recovery characteristics over the inlet throat Mach number range investigated (Fig. 2a) and agreed very well with experimental measurements. However, differences between the FNS and RNS solutions were observed when comparing the circumferential distortion as measured in terms of the DC_{60} engine face descriptor (Fig. 2b). Although these differences are relatively small, they can be attributed to a number of factors including 1) the different turbulence model used in computer codes, 2) artificial viscosity used in the FNS analysis which could influence the flow physics of vortex liftoff, and 3) the influence of the Deiwert approximation in the FNS analysis. Convergence with this variant of PARC3D could not be achieved without the Diewert approximation. However this modification to the Baldwin-Lomax turbulence model destroyed the flow physics of the liftoff topology.

Above an inlet throat Mach number of 0.4, the two solution techniques gave essentially the same qualitative behavior, i.e., an increasing DC_{60} engine distortion with increasing throat Mach number. However, below a throat Mach number of 0.4, the two solutions techniques indicated opposite trends with inlet throat Mach number. The RNS solution indicated very good agreement with experimental measurements, whereas

the FNS solution tended to indicate a somewhat larger DC_{60} engine face circumferential distortion than is indicated by the data above an inlet throat Mach number of 0.4. The generally good averaged inlet performance results that were obtained with both the FNS and RNS solution techniques obtained for the M2129 inlet S-duct should be viewed with caution, since not all of the inlet flow physics were well predicted by either Navier-Stokes solution techniques as the following discussion will indicate.

Both the FNS and RNS analysis indicated that the M2129 inlet flow separated over the nominal Mach number range from 0.2 to 0.8. The location of separation, as determined from both the FNS and RNS solution techniques, is presented in Fig. 3, and suggests that some of the computed differences in the DC_{60} engine face distortion indicated in Fig. 3 can be attributed to differences in the prediction of flow separation location within the inlet duct. Figure 3 also indicates that the location of flow separation is effected by inlet throat Mach number, and that no consistent statement can be made as to the prediction of separation using either FNS or RNS solution techniques over the inlet mass flow range considered in the experiment. However, both computational techniques using current mixing length type turbulence models predicted separation much further downstream in the inlet duct than was measured using oil flow techniques.[20] Grid resolution studies performed using RNS3D revealed little change in the vortex liftoff location as a result of either refining the computational mesh or further resolving the near wall region. Resolution studies were not performed using the FNS analysis because of the large resources involved. In general, the RNS and FNS solution techniques were more consistent with each other than with the experimentally measured separation locations. Thus, it is unlikely that the current generation of mixing length turbulence models can predict the conditions under which the vortex pair that is generated in the first section of the S-duct will liftoff the walls of the inlet.

Presented in Figs. 4–6 are measured and the computed engine face total pressure recovery maps for the test case 3.1 and 3.2 initial conditions. Figure 4 presents a comparison between the measured recovery maps for the test case 3.1 and 3.2 inlet flow conditions (Figs. 4a and 4b), respectively. Figures 5 and 6 present a comparison between the predicted

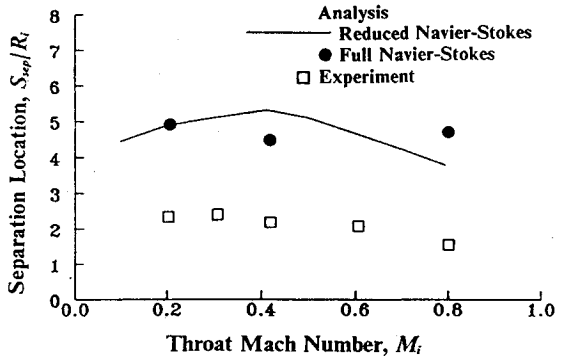

Fig. 3 Effect of inlet throat Mach number on the location of flow separation S_{sep}/R_i, M2129 inlet S-duct.

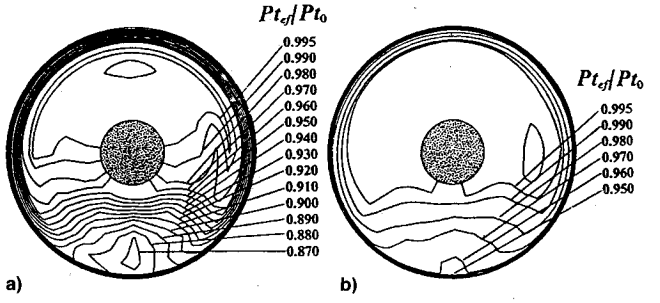

Fig. 4 Measured engine face total pressure recovery map, M2129 inlet S-duct. Test case a) 3.1 and b) 3.2 conditions.

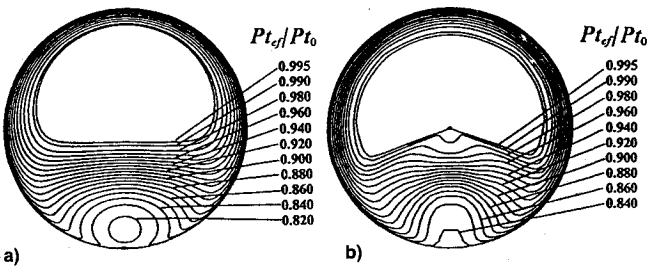

Fig. 5 Computed engine face total pressure recovery map, M2129 inlet S-duct. Test case 3.1 conditions: a) RNS and b) FNS analysis.

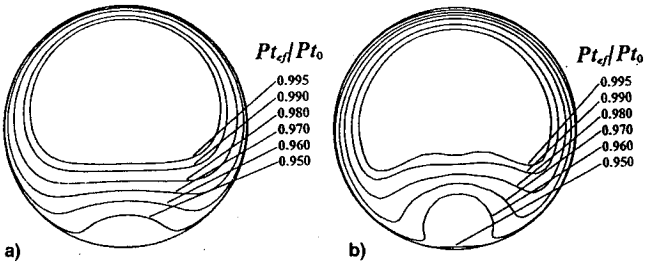

Fig. 6 Computed engine face total pressure recovery map, M2129 inlet S-duct. Test case 3.2 conditions: a) RNS and b) FNS analysis.

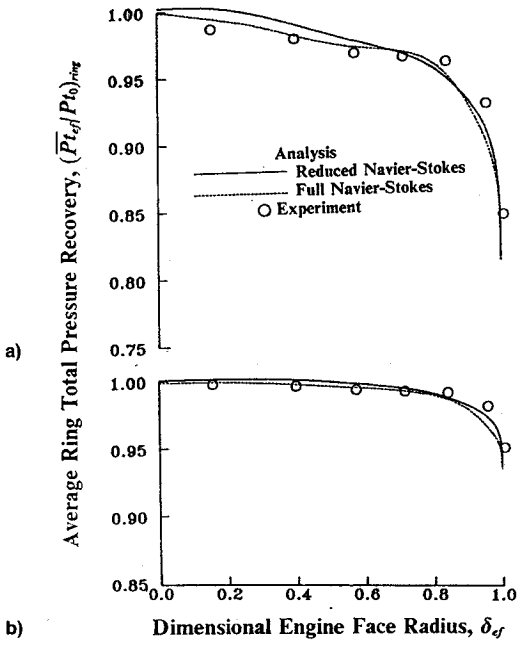

Fig. 7 Average ring total pressure recovery characteristics, M2129 inlet S-duct. Test case a) 3.1 and b) 3.2 conditions.

engine face total pressure recovery map using both RNS and FNS solution techniques at the test case 3.1, and 3.2 initial flow conditions. In general, there is strong similarity between the engine face flowfield as computed by the two Navier-Stokes techniques, although the FNS solution at the test case 3.1 and 3.2 flow conditions indicated a somewhat more developed recovery map as a result of stronger secondary velocities. The more developed engine face flowfield computed by the FNS analysis is indicated in Fig. 2b as a higher DC_{60} engine face distortion. In general, there was good qualitative agreement between the two analysis techniques and the experimental data with regard to the engine face total pressure recover maps, although the vortex appears to have altered the flow over a greater region of the engine face flowfield in the experiment than in the analyses for the test case 3.1 initial conditions (Fig. 4a).

The quantitative nature of the computed differences between the FNS and RNS solutions technique are revealed more clearly in Figs. 7–9, which presents the average ring

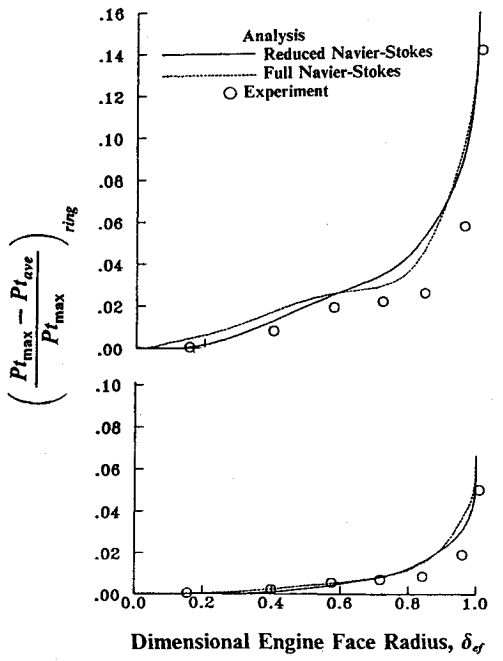

Fig. 8 Radial pressure ring distortion characteristics, M2129 inlet S-duct. Test case a) 3.1 and b) 3.2 conditions.

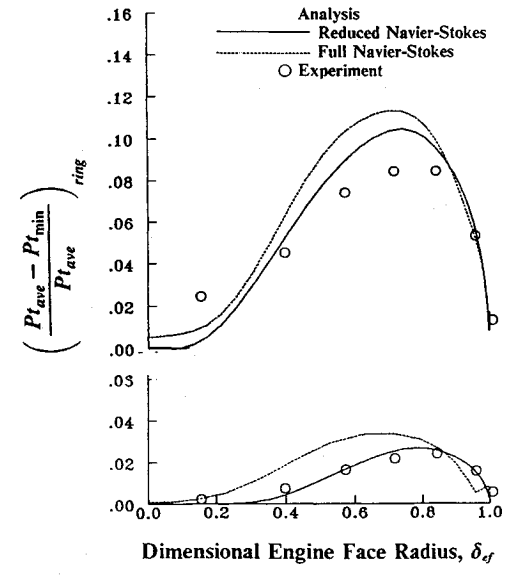

Fig. 9 60-deg sector circumferential pressure ring distortion characteristics, M2129 inlet S-duct. Test case a) 3.1 and b) 3.2 conditions.

total pressure recovery characteristics (Fig. 7), the radial pressure ring distortion distribution (Fig. 8), and the 60-deg sector circumferential ring distortion characteristics (Fig. 9) for the test case 3.1 and 3.2 flow conditions. These ring parameters are very useful in quantifying difference because they describe the distribution of total pressure recovery, radial distortion, and circumferential distortion in terms of the fractional distance across the engine face flowfield δ_{ef}. The distribution of average ring total pressure recovery (Figs. 7a and 7b) are predicted remarkably well by both the RNS and FNS analyses for the test case 3.1 and 3.2 flow conditions. However, the analyses tended to overpredict the total pressure recovery in the engine face center region while underpredicting the pressure recovery in the outer region near the engine face, suggesting that more mixing had taken place in the experimental inlet duct. The radial pressure ring distortion as computed by both Navier-Stokes techniques are presented if Fig. 8a for the test case 3.1 flow conditions and in Fig. 8b for the test case 3.2 conditions. The underprediction of the total pressure recovery in the region near the engine face casing is indicated in Figs. 8a and 8b as an overprediction in radial distortion in the same region of engine face flowfield. The primary differences in the prediction of flow separation computed by FNS and RNS analyses as compared to experimental measurements shows itself as a difference in circumferential pressure distortion as indicated in Figs. 9a and 9b. At the test case 3.1 flow conditions (Fig. 9a), both the RNS and FNS analyses overpredicted the maximum 60-deg engine face ring distortion, although the analyses predicted the overall distribution quite well including the location of maximum distortion at 0.8 of the engine face dimensional radius δ_{ef}. At the test case 3.2 flow conditions (Fig. 9b), the RNS analyses predicted the 60-deg sector ring distortion very well, whereas the FNS analysis overpredicted the maximum circumferential distortion by about 1.0%.

If agreement between solution techniques is measured in terms of the standard inlet parameters such as total pressure recovery and the standard engine face distortion descriptors, then the two Navier-Stokes analyses gave remarkably similar results for a inlet duct experiencing flow separation characterized as vortex liftoff, and agreed reasonably well with experimental measurements. However, the FNS and RNS also predicted separation much further downstream in the M2129 inlet S-duct than was indicated by experimental data. This is consistent with the results of the FNS analysis of separation in an S-duct by Harlof et al.[3]

Once the vortex pair have detached from the walls of the inlet duct, they no longer can be strengthened by the generation of secondary flow, and they must be attenuated by diffusion, mixing, and viscous dissipation. Diffusion tends to enlarge the region of total pressure distortion thus leading to increased distortion level, while forced mixing and viscous dissipation tend to attenuate total pressure gradients which will decrease engine face distortion. Thus, an inlet S-duct configuration which experiences separation sooner will on the one hand be expected to have a higher distortion because of diffusion, but on the other will tend to have a lower distortion because of the moderating effects of mixing and viscous dissipation over the longer length of free vortex travel. Therefore, the physical process involved in the phenomenon of vortex liftoff tends to be self-compensating with respect to engine face distortion. The two Navier-Stokes computations predicted averaged performance parameters at the engine face remarkably well. The fact that the analyses predicted vortex liftoff much further downstream in the M2129 inlet duct than was measured indicates that while the accumulative effect of diffusion, mixing, and viscous dissipation were nearly the same between analysis and data, the individual terms could not have been accurately predicted. This may have resulted from a lack of grid resolution in both the RNS and FNS analysis, particularly downstream of vortex liftoff.

Presented in Figs. 10 and 11 are a comparison between measured and computed wall static pressure along the θ = 0.0 deg, and θ = 180.0 deg surface elements for the test case 3.1 initial conditions (Fig. 10) and the test case 3.2 flow conditions (Fig. 11). The static pressures distributions as determined from the FNS and RNS solution technique are in surprising agreement (Figs. 10 and 11). However, since both solutions techniques predicted the vortex liftoff (separation) location further downstream than was measured by Gibb and Jackson,[20] the differences between the computed and measured static pressure distributions are greater than the difference between the wall pressure distributions obtained with the RNS and FNS solution techniques. In addition to overpredicting the vortex liftoff position within the M2129 inlet S-duct, the two solution techniques also underpredicted the influence of the separation on the main flow as indicated by the wall static pressure distribution at the test case 3.1 flow conditions (Fig. 10). Since the separation region associated with vortex liftoff was very thin, the vortex pressure field interaction was probably more complex than a simple bound-

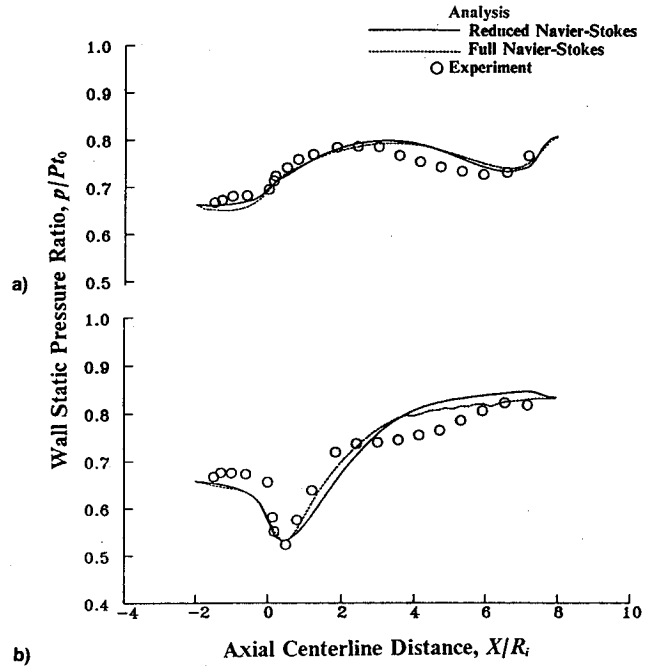

Fig. 10 Static pressure distribution, M2129 inlet S-duct, test case 3.1 initial conditions. θ = a) 0.0- and b) 180.0-deg surface elements.

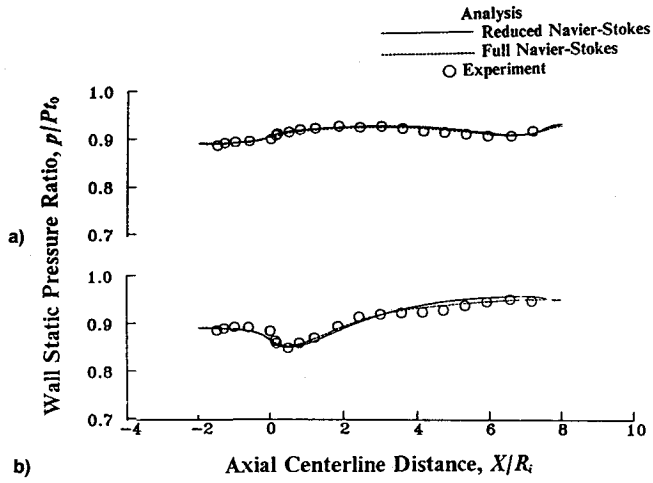

Fig. 11 Static pressure distribution, M2129 inlet S-duct, test case 3.2 initial conditions. θ = a) 0.0- and b) 180.0-deg surface elements.

ary-layer displacement effect. The fact that Navier-Stokes solutions tend to underpredict the effect of separation (vortex liftoff) on the main flowfield was also indicated in the study by Harlof et al.[3] However, the RNS and FNS wall static pressure distribution results are in much better agreement with measured wall static pressure distributions at the test case 3.2 initial conditions (Fig. 11) suggesting that the pressure liftoff interaction weakens as the inlet throat Mach number decreases.

The major difference between FNS and RNS solutions occur in the wall skin friction distribution upstream of flow separation, i.e., the region of adverse pressure gradients in the first section of the S-duct at the test case 3.1 and 3.2 initial flow conditions, Figs. 12a and 12b. Except for the initial expansion region at the entrance of the M2129 inlet S-duct, the skin friction distribution computed from RNS and FNS solution techniques are essentially the same at the test case 3.3 flow conditions (Fig. 12c). The skin friction in the separated region is characterized as very constant and very close to zero for both analysis techniques. This is consistent with the results obtained by Harlof et al., and indicates that the reverse flow velocity was very small. This is in agreement with

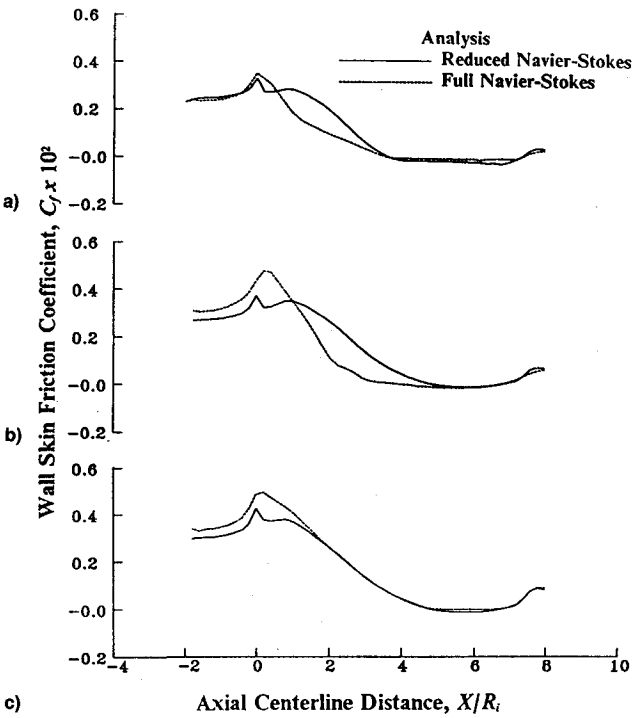

Fig. 12 Wall skin friction distribution along the θ = 180 deg surface element. Test case a) 3.1, b) 3.2, and c) 3.3 conditions.

Fig. 13 Reduced Navier-Stokes solution for the separation topology associated with vortex liftoff.

ec the experimental measurements of Whitelaw and Yu[21] within the M2129 inlet S-duct.

Presented in Fig. 13 is the RNS solution for the separation topology associated with vortex liftoff. A very striking and significant feature captured by the RNS analysis is the symmetric pair of spiral nodes and pair of saddle points that are clearly indicated in Fig. 13. A detailed discussion on the topology of vortex liftoff as computed using an RNS analysis is given by Anderson and Farokhi.[4] This very familiar topological pattern describes the important stage in the development of the pair of counter rotating vortices that form in the first bend of the inlet duct which results in vortex liftoff in the second bend. This limiting streamline topology must be present under the conditions of flow separation characterized as vortex liftoff. The Deiwert approximation[17] used in the FNS analysis, however, destroyed this familiar topological pattern and should not be used for internal flows of this type.

The development of the separated region is similar in all the RNS cases, but the separated region occupies an increasingly greater area as the inlet mass flow increases. The radial extent of the reverse flow is small over the inlet mass flow range considered and the magnitude of the negative velocities near zero so that the separated flow might be regarded as incipient. Since the liftoff topology flow physics was properly

simulated with the RNS analysis, the parabolized form of the Navier-Stokes equations is appropriate for the type of separated flows represented by the M2129 inlet S-duct. The same conclusion was reached by Whitelaw and Yu[21] in a low Reynolds number laser velocimeter experiment in the M2129 S-duct.

Concluding Remarks

A three-dimensional implicit FNS analysis and a three-dimensional RNS initial value space marching solution technique has been applied to a class of separated flow problems within a diffusing S-duct configuration characterized as vortex liftoff. Both the FNS and the RNS solution techniques were able to capture the overall flow physics of vortex liftoff, and gave remarkably similar results which agreed reasonably well with the experimental measured averaged performance parameters of engine face total pressure recovery and distortion. However, the FNS and RNS also predicted separation much further downstream in the M2129 inlet S-duct than was indicated by experimental data, suggesting compensating errors were present which may have been grid related.

The separated region associated with vortex liftoff in M2129 inlet S-duct increased in size as the inlet mass flow increased, although the radial extent of the reverse flow region remained very small. Since the reverse flow velocity was also very small, the separated flow in the M2129 S-duct might be regarded as incipient. This, along with the fact that the RNS analysis was able to capture the topology of vortex liftoff and provide good agreement with the experimentally measured performance, indicates that the parabolized form of the Navier-Stokes equations are appropriate for separated flows represented by the M2129 inlet S-duct. The fact that the location of vortex liftoff was not properly predicted does not alter this conclusion, since the FNS analysis suffers the very same difficulty.

References

[1]Advisory Group for Aerospace Research and Development (AGARD), "Engine Response to Distorted Inflow Conditions," AGARD CP-400, Munich, Germany, Sept. 1986.

[2]Bowditch, D. N., and Coltrin, R. E., "A Survey of Inlet/Engine Distortion Compatibility," AIAA Paper 83-1166, June 1983.

[3]Harlof, G. J., Reichert, B. A., and Wellborn, S. R., "Navier-Stokes Analysis and Experimental Data Comparison of Compressible Flow in Diffusing S-Duct," AIAA Paper 92-2699, June 1992.

[4]Anderson, B. H., and Farokhi, S., "A Study of Three Dimensional Turbulent Boundary Layer Separation and Vortex Flow Control Using the Reduced Navier Stokes Equations," Turbulent Shear Flow Symposium, Munich, Germany, Sept. 1991.

[5]Briley, W. R., and McDonald, H., "Analysis and Computation of Viscous Subsonic Primary and Secondary Flow," AIAA Paper 79-1453, Jan. 1979.

[6]Briley, W. R., and McDonald, H., "Three-Dimensional Viscous Flows with Large Secondary Velocities," *Journal of Fluid Mechanics*, Vol. 144, March 1984, pp. 47–77.

[7]Levy, R., Briley, W. R., and McDonald, H., "Viscous Primary/Secondary Flow Analysis for Use with Nonorthogonal Coordinate Systems," AIAA Paper 83-0556, Jan. 1983.

[8]Anderson, B. H., "The Aerodynamic Characteristics of Vortex Ingestion for the F/A-18 Inlet Duct," AIAA Paper 91-0130, Jan. 1991.

[9]McDonald, H., and Camarata, F. J., "An Extended Mixing Length for Computing the Turbulent Boundary-Layer Development, Proceedings, Stanford Conference of Turbulent Boundary Layers," Vol. I, Stanford Univ., Stanford, CA, 1969, pp. 83–98.

[10]Reyhner, T. A., and Flugge-Lotz, I., "Interaction of a Shock Wave with a Laminar Boundary Layer," *Internal Journal of Non-Linear Mechanics*, Vol. 3, 1968.

[11]Cooper, G. K., "The PARC Codes," Arnold Engineering Development Center, AEDC-TR-87-24, Tullahoma, TN, Oct. 1987.

[12]Pulliam, T. H., and Steger, J. L., "Implicit Finite-Difference Simulation of Three-Dimensional Compressible Flow," *AIAA Journal*, Vol. 18, No. 2, 1980, pp. 159–167.

[13]Pulliam, T. H., "Euler and Thin Navier-Stokes Codes: ARC2D, ARC3D," Notes for Computational Fluid Dynamics User's Workshops, Univ. of Tennessee Space Inst., UTSI Pub. E02-4005-023-84, Tullahoma, TN, 1984, pp. 15.1–15.85.

[14]Jameson, A., Schmidt, W., and Turkel, E., "Numerical Solutions of the Euler Equations by Finite-Volume Methods Using Runge-Kutta Time-Stepping Schemes," AIAA Paper 81-1259, June 1981.

[15]Pulliam, T. H., and Chaussee, D. S., "A Diagonal Form of an Implicit Approximate Factorization Algorithm," *Journal of Computational Physics*, Vol. 39, 1981, pp. 347–363.

[16]Baldwin, B., and Lomax, H., "Thin-Layer Approximation and Algebric Model for Separated Flows," AIAA Paper 78-257, Jan. 1978.

[17]Deiwert, G. S., "Computation of Separated Transonic Turbulent Flows," *AIAA Journal*, Vol. 14, No. 6, 1976, pp. 735–740.

[18]Advisory Group for Aerospace Research and Development (AGARD), "Air Intakes for High Speed Vehicles," Fluid Dynamics Panel Working Group 13, AR-270, Fort Worth, TX, Sept. 1991.

[19]Willmer, A. C., Brown, T. W., and Goldsmith, E. L., "Effects of Intake Geometry on Circular Pitot Intake Performance at Zero and Low Forward Speeds," *Aerodynamics of Power Plant Installation* (Toulouse, France), May 1981, pp. 5-1–5-16 (AGARD CP301, Paper 5).

[20]Gibb, J., and Jackson, M., "Some Preliminary Results from Tests Using Vortex Generators in the Circular/Circular Diffusing S-Duct Model M2129 Test Phase 3," Defence Research Agency Rept. AP4(92)WP15, Aug. 1992.

[21]Whitelaw, J. H., and Yu, S. C., "Velocity Measurements in an S-Shaped Duct," *Experiments in Fluids*, Vol. 15, 1993, pp. 364–367.